World Scientific
www.worldscientific.com

Site Occupancy, Surface Morphology and Mechanical Properties of Ce³⁺ Added Ni–Mn–Zn Ferrite Nanocrystals Synthesized Via Sol–Gel Route

Vikram More[*], R. B. Borade[†], Kirti Desai[‡], V. K. Barote[§], S. S. Kadam[¶],
V. S. Shinde[∥], D. R. Kulkarni[**], R. H. Kadam[¶,††] and S. T. Alone[*]

*Department of Physics, Rajarshi Shahu College
Pathri, Aurangabad District, Maharashtra, India

†Department of Physics, Ankushrao Tope College
Jalna, Maharashtra, India

‡Department of Physics, Balbhim College
Beed, Maharashtra, India

§Department of Physics, Sant Dnyaneshwar College
Soegaon, Aurangabad District
Maharashtra, India

¶Department of Physics, Shrikrishna College
Gunjoti, Osmanabad District,
Maharashtra, India

∥Department of Chemistry, Shivaji College
Omerga, Osmanabad District
Maharashtra, India

**Department of Chemistry, Shrikrishna College
Gunjoti, Osmanabad District
Maharashtra, India
††ram111612@yahoo.co.in

Ferrite nanoparticles of $Ni_{0.35}Mn_{0.35}Zn_{0.3}Fe_{2-x}Ce_xO_4$ ferrite system were produced using sol–gel auto combustion technique. X-ray diffraction analysis confirms the single phase cubic spinel structure of the samples with space group Fd-3m. Replacement of Fe^{3+} ions by Ce^{3+} ions increases the lattice parameter 8.4105 Å to 8.4193. Average crystallite size obtained from Scherrer method varies from 21.73 nm to 22.71 nm with replacement of Fe^{3+} ions by Ce^{3+} ions. Williamson–Hall and strain-size plot analysis confirms the nanocrystalline nature of the samples and the micro-strain induced in the cubic crystals is of tensile type. Cation distribution suggests that

††Corresponding author.

Zn^{2+} ions occupy tetrahedral — A-site while Ni^{2+} ions occupy octahedral — B-site. Majority of the Mn^{2+} ions prefer A-site and majority of the Ce^{3+} ions replace Fe^{3+} ions at octahedral — B-site. High resolution transmission images confirm the homogeneity and nanoparticle nature of the samples. Two main characteristics absorption bands corresponding to spine structure are observed in the Fourier transmission infra-red spectra within the wavenumber range of 350–600 cm^{-1}. Stiffness constant, Young's modulus, rigidity modulus, bulk modulus and Debye temperature were estimated using FTIR data. Debye temperature obtained from the Waldron equation varies from 676 K to 692 K with the addition of Ce^{3+} ions. Higher values of elastic moduli are suitable for industrial applications due to increased mechanical strength.

1. Introduction

Mixed Ni–Zn and Mn–Zn ferrites have been extensively investigated from their application point of view in various technological fields.[1,2] Variety of applications led the ferrite materials as one of the important materials. They possess in the field of science and technology.[3–7] Both Ni–Zn and Mn–Zn ferrites are known for their soft magnetic properties. They possess high electrical resistance ($\sim 10^7 \,\Omega$.cm) as well as high permeability in radio frequency (RF) region and low losses of eddy currents within the frequency range 10–500 MHz.[8–11] In the recent past, several researchers have reported the micro-structure, cation distribution, morphological, magnetic and electrical properties of Ni–Mn–Zn ferrites doped by various divalent and trivalent metal ions.[1–3,11–13] Magnetic behavior of ferrites has been paid considerable attention due to their improvement in the overall magnetic properties.[14–16] Improvements in structural and magnetic and electrical properties of the ferrites at nanoscale dimension still have the top priority in order to fabricate the micro-devices at low cost.[17] The physical and chemical properties of spinel ferrites can easily be tuned by adding appropriate amount of dopant and by changing the synthesis route and sintering conditions. Replacement of Fe^{3+} ions in spinel ferrite by fractional amount of rare earth ions alters the structural, magnetic and electrical properties. Rare earth ions with higher ionic radii than Fe^{3+} ions have limited solubility in the spinel lattice.[18] Introduction of rare earth ions in spinel ferrites easily induces the increasing ionic radii, micro-strain and controlled magnetic properties. Strong spin–orbit coupling of unpaired 4f electrons in rare earth ions enhances the electric and magnetic properties of the ferrites.[19] Furthermore, the most significant factor for the

modification of structural and magnetic parameters is the replacement of Fe^{3+} ions by rare earth elements having relatively larger ionic radii.[20] Literature reports suggest that enhanced electrical and magnetic properties of Ce^{3+}-doped spinel ferrites have significant applications in different areas such as biomedical, sensing and core-switching.[17,18,21,22]

Below the critical size, ferromagnetic materials are single domain particles and show high saturation magnetization. Hence, the type of cation impurity is added, its site occupancy and size of the crystallites extensively influence the electrical and magnetic properties of ferrites.[23] A spinel ferrite possesses cubic crystal geometry belonging to the space group Fd-3m. Occupancy of divalent cation such as Mg^{2+}, Mn^{2+}, Zn^{2+}, Ni^{2+}, Co^{2+} and Cu^{2+} over both tetrahedral — A and octahedral — B sites is termed as mixed (random) spinel ferrites. Ni-Mn–Zn ferrites also fall under this category.[1] It is a challenging job to predict the possible site occupancies of metal cations in multi-ionic mixed ferrites. Site preferences by metal cations towards tetrahedral — A and octahedral — B sites are also governed by synthesis approaches and synthesis conditions.[24] Several synthesis approaches have been developed in order to control the particle size at nanoscale dimension and to achieve the desired properties.[25–27] Despite the several synthesis techniques, sol–gel auto-combustion technique produces nanoparticles with promising control on size and shape of particles. This synthesis approach is able to produce the homogeneous nanosized particles at low temperature and low cost. The main objective of this investigation is to investigate the micro-structural, site occupancy, surface morphology and mechanical properties of Ni$_{0.35}$Mn$_{0.35}$Zn$_{0.3}$Fe$_{2-x}$Ce$_x$O$_4$. All the ferrite nanoparticles were obtained via

Table 1. Molecular mass of $Ni_{0.35}Mn_{0.35}Zn_{0.3}Fe_{2-x}Ce_xO_4$.

| Comp. 'x' | Molar mass (g/mol element) | | | | | | Total (g/mol compound) |
	Ni	Mn	Zn	Fe	Ce	O	
0.0	20.5	19.2	19.614	111.694	0.000	63.996	235.077
0.025	20.5	19.2	19.614	110.298	2.603	63.996	236.284
0.050	20.5	19.2	19.614	108.902	5.206	63.996	237.491
0.075	20.5	19.2	19.614	107.505	7.809	63.996	238.698
0.1	20.5	19.2	19.614	106.109	10.412	63.996	239.905

sol–gel technique by using the metal nitrates of constituent elements as precursors.

2. Experimental

Polycrystalline nanoparticles of $Ni_{0.35}Mn_{0.35}Zn_{0.3}$-$Fe_{2-x}Ce_xO_4$ ($x = 0.0, 0.025, 0.050, 0.075$ and 0.1) were synthesized using sol–gel auto-ignition process. High purity ($>98.5\%$) metal nitrates $Ni(NO_3)_2 \cdot H_{12}O_6$, $Mn(NO_3)_2 \cdot H_{12}O_6$, $Zn(NO_3)_2 \cdot H_{12}O_6$, $Fe(NO_3)_3 \cdot H_{18}O_9$ and $Ce(NO_3)_3 \cdot H_{18}O_9$ were used as initial materials. Table 1 represents the molar mass of the reagents used in the synthesis. Double distilled demonized water was used to dissolve the starting materials with their stoichiometric proportion. The mixed solution was continuously stirred by maintaining the constant temperature of 90°C. Citric acid was mixed in the nitrates solution with the ratio of 1:3 of metal nitrate to citrate. The pH of the solution was kept constant at 7 by slowly adding the liquid ammonia in the solution. Continuous stirring at constant pH and temperature for 2–3 h converts the solution in to viscous gel. After half an hour, the dark brown gel was burnt by self-ignition process and converted into brown ash. The grinded ash powders were sintered at 900°C for 6 h in order to obtain the final products. The as-prepared samples were investigated by X-ray diffraction (XRD) technique, transmission electron microscopy (TEM) and Fourier Transform Infrared Spectroscopy. Powder XRD technique was adopted to obtain the XRD patterns at room temperature within the 2θ range of 20–80°. Cu-k$_\alpha$ radiation having the incident wavelength $\lambda = 1.5406$ Å were used. High resolution transmission electron micrographs were recorded by using 200 kV TEM model (Philips CM-200). Room temperature Fourier transform infrared spectra of all the samples were recorded on the disc shaped samples in the wave number range of 350–4000 cm^{-1} by using

the infrared spectrometer (Model 783, Perkin Elmer).

3. Results and Discussion

Powder XRD patterns of $Ni_{0.35}Mn_{0.35}Zn_{0.3}$-$Fe_{2-x}Ce_xO_4$ ($x = 0.0, 0.025, 0.050, 0.075, 1.0$) are shown in Fig. 1. For all the samples, Bragg's lines were observed near the angular positions 30.03, 35.34, 36.97, 42.95, 53.28, 56.80, 62.37 and 73.77°. Bragg's positions show minor shifting towards lower 2θ angles with the substitution of Ce^{3+} ions. All Bragg's lines are well indexed by the planes (220), (311), (222), (400), (422), (333), (440), (620), (533) and (622). Indexed peaks confirm the single phase cubic crystal geometry of the samples. Absence of any un-indexed peak confirms the phase purity of the samples. All XRD lines are matched well with the results from international database (COD card No. 90-900-6895, Space group: Fd-3m). Sharp and intensive peaks confirm the crystallinity of the samples. Lattice constant 'a' of each sample was
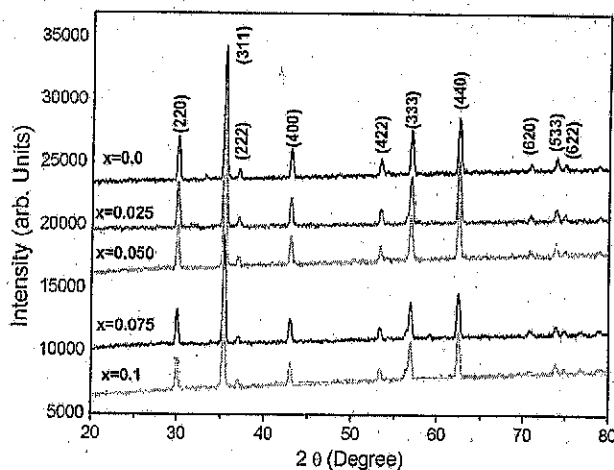

Fig. 1. Room temperature powder X-ray diffraction patterns of $Ni_{0.35}Mn_{0.35}Zn_{0.3}Fe_{2-x}Ce_xO_4$.

Table 2. Lattice parameter (a), Crystallite size (t) and lattice strain (ε) of $Ni_{0.35}Mn_{0.35}Zn_{0.3}Fe_{2-x}Ce_xO_4$.

'x'	'a' (Å)	Scherrer method	W–H Method		SSP Method	
		't_{D-S}' (nm)	't_{W-H}' (nm)	$\varepsilon \times 10^{-4}$	't_{SSP}' (nm)	$\varepsilon \times 10^{-4}$
0.0	8.4105	21.73	24.13	2.52	24.46	1.36
0.025	8.4135	21.78	24.34	2.68	24.88	1.86
0.050	8.4142	21.89	24.75	3.05	25.17	2.43
0.075	8.4185	22.24	25.23	3.38	25.79	2.91
0.1	8.4193	22.71	26.47	3.96	26.33	3.17

estimated by using the relation discussed elsewhere.[28] The addition of Ce^{3+} ions increases the lattice constant from 8.4105 Å to 8.4193 Å (Table 2) obeying Vegard's law.[29] The expansion in crystal lattice is completely related to the replacement of smaller Fe^{3+} ions (ionic radii 0.67 Å) by the comparatively larger Ce^{3+} ions (ionic radii 1.01 Å).[17] Phase purity of the doped samples confirmed that the Ce^{3+} ions are successfully entered in the Ni–Mn–Zn–Fe–O crystal lattice. Comparatively larger ionic radii of Ce^{3+} ions expand the lattice spacing.

By using Bragg's positions and peak broadenings (FWHM) in Debye–Scherrer equation, the average crystallite size of all the samples was estimated[30] as follows:

$$t_{D-S} = \frac{K\lambda}{\beta_{hkl}Cos\theta_B}. \qquad (1)$$

It can be seen from Table 2 that the average crystallite size obtained from above equation increases from 21.73 nm to 22.71 nm with the increasing concentration of Ce^{3+} ions. The error occurred due to the combined effect of physical and instrumental line broadenings can be minimized by employing the following relation[31]:

$$\beta_{Corr}^2 = \beta_{Phy}^2 - \beta_{Inst}^2, \qquad (2)$$

where $\beta_{Corr.}$ is the corrected line broadening while $\beta_{Phy.}$ and $\beta_{Inst.}$ are the physical and instrumental line broadenings. Point defects, grain boundary widths, triple junctions and stacking faults develop the strain inside the crystal lattice.[32] The Scherrer equation focuses mainly on the crystallite size effect on the line broadening. Micro-strain induced in the crystal lattice is not considered in Scherrer equation. Williamson–Hall analysis is one of the popular methods which considers both size and strain effect on line broadening.[33,34] The physical line broadening of the diffraction peaks is the combined effect of

size and strain. Hence, the strain can be obtained by using the following relation[35]:

$$\varepsilon = \frac{\beta_{Res}}{4\tan\theta}, \qquad (3)$$

where ε represents the strain induced and β_{Res} is the resultant peak broadening. The resultant broadening can be obtained from the summation of line broadening due to crystallite size and micro-strain induced.[36] By considering the size and strain broadenings, Scherrer equation can be modified as follows[37]:

$$\beta_{hkl}Cos\theta = \frac{K\lambda}{t_{W-H}} + 4\varepsilon Sin\theta, \qquad (4)$$

where K is Scherrer constant, λ is the wavelength of incident X-ray's, t_{W-H} is the crystallite size, β_{hkl} is the full width of diffraction peak at its maximum height and θ is the peak position. Equation (4) can be referred as W–H equation which gives the more precise values of crystallite size and micro-strain induced in the crystal lattice. Figure 2 represents the W–H plots drawn between $\beta_{hkl}Cos\theta$ and $4Sin\theta$. Slopes of linearly fitted lines give the micro-strain induced in the crystal lattice while Y-intercept gives the values of crystallite size. Crystallite size (t_{W-H}) obtained from W–H analysis is found in the range 24.13–26.47 nm and fairly matches with the Scherrer method. Lattice strain induced in the crystal lattice increases from 2.52×10^{-4} to 3.96×10^{-4} with the addition of Ce^{3+} ions and the values are represented in Table 2. Positive strain values indicating the tensile type of induced strain and its variation are analogues with the lattice lengths variation.[38] The crystal lattices are expected to extend infinity in all directions which is not feasible for the crystals with finite size. W–H analysis is based on isotropic nature of line broadening which indicates that the
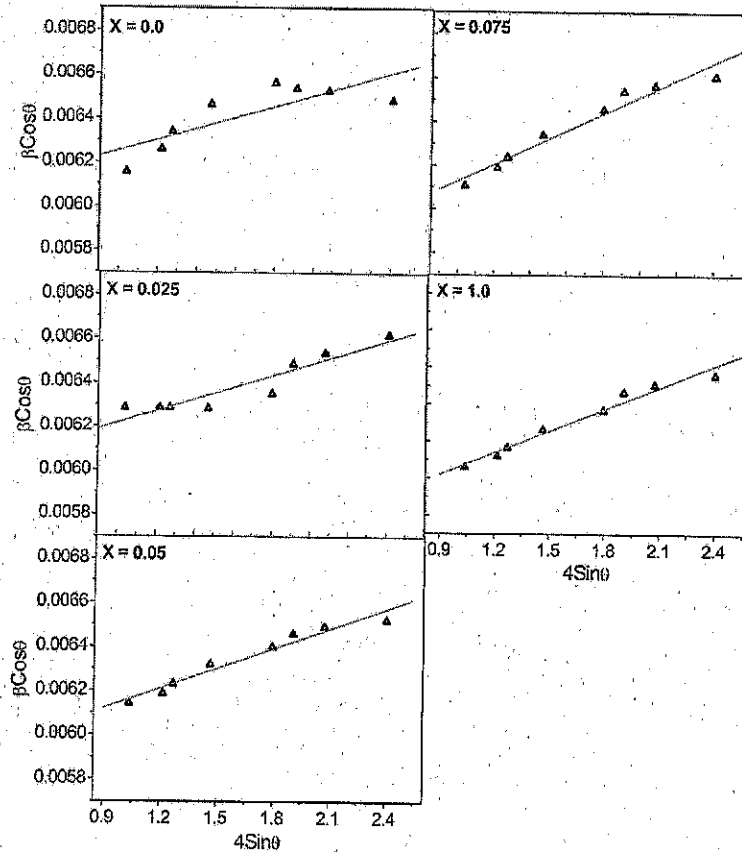
Fig. 2. W–H plots of $Ni_{0.35}Mn_{0.35}Zn_{0.3}Fe_{2-x}Ce_xO_4$.

diffraction domains are also isotropic.[39] Size-strain plot method is another method which gives the better information of size and strain. This method gives less weightage for higher angle reflections where the accuracy is relatively lower. Lorentz's function and Gaussian function are assumed to describe the size and strain profile, respectively, in SSP method, which can be given by the following relation[40]:

$$(d_{hkl}\beta_{hkl}Cos\theta)^2 = \frac{k\lambda}{t_{SSP}}(d_{hkl}^2\beta_{hkl}Cos\theta) + \left(\frac{\varepsilon}{2}\right)^2, \quad (5)$$

where d_{hkl} and β_{hkl} are the corresponding values of interplaner spacing and FWHM for selected plane. Figure 3 shows the variation of $(d_{hkl}^2\beta_{hkl}Cos\theta)$ versus $(d_{hkl}\beta_{hkl}Cos\theta)^2$ for all the samples of Ce-doped Ni–Mn–Zn ferrites. Slopes of linearly fitted straight lines give the values of crystallites size and Y-intercept gives lattice strains (Table 2). Values of crystallite size and lattice strain obtained from SSP method are in good agreement with the Scherrer and W–H methods.

Physical properties of ferrites with spinel structure are strongly susceptible to the type of cations and their preferences towards tetrahedral — A and octahedral — B sites. In order to understand the electrical and magnetic behavior of spinel ferrites, knowledge of site preference is very essential.[41] In this investigation, cation distribution is based on the considerations that, (i) due to inverse structure Ni^{2+} ions prefers B-site, (ii) normal Zn^{2+} ions prefers A-site and (iii) due to large ionic radii Ce^{3+} ions replaces Fe^{3+} ions at octahedral site. Among the several spectroscopic techniques available for cation distribution, XRD technique is used widely in which knowledge of peak intensity describes the cation distribution.[42] According to this method, few pairs of intensity peaks were selected which are sensitive to cation distribution.[43]

$$\frac{I_{hkl}^{Obs}}{I_{h'k'l'}^{Obs}} = \frac{I_{hkl}^{Cal}}{I_{h'k'l'}^{Cal}}, \quad (6)$$

where I_{hkl}^{Obs} and I_{hkl}^{Cal} are the observed and calculated intensity values selected planes. The intensity pairs
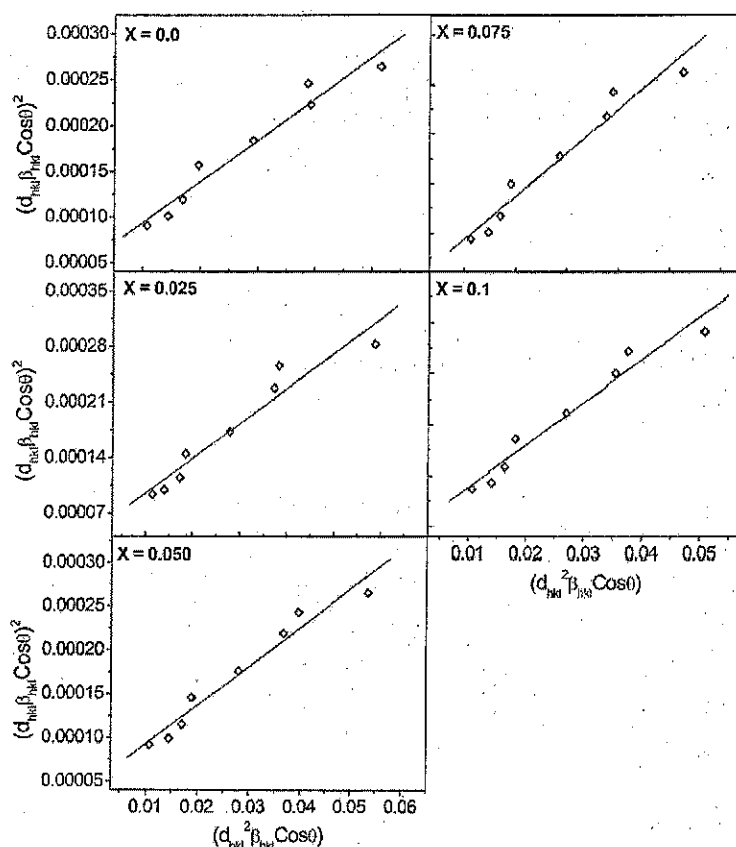
Fig. 3.   SSP plots of $Ni_{0.35}Mn_{0.35}Zn_{0.3}Fe_{2-x}Ce_xO_4$.

were selected in order to achieve the best information of cation occupancy over tetrahedral — A and octahedral — B sites. Only those peaks were selected whose intensities are not dependent on oxygen parameter and changes in opposite direction with the cation distribution.[44] For these investigated samples, the cation distribution was obtained by considering the intensity ratios (220/400), (400/422) and (220/422) which are assumed to be sensitive for site occupancies. The relative integrated intensity (I_{hkl}) can be obtained by using the following relation:

$$I_{hkl} = |F_{hkl}|^2 \cdot P \cdot L_p, \qquad (7)$$

where F_{hkl} is the structure factor, P is the multiplicity factor and L_p is the Lorentz-polarization factor. Literature values of atomic scattering factors of various ions were used for intensity calculations.[45] To obtain more accurate comparison between observed and calculated intensities, a suitable correction in the principle is necessary because the observed intensities are obtained at room

temperature and calculated intensities are valid at $0\,K$.[46] However, due to high melting point, thermal variations of spinel atoms at room temperature show negligible difference to that at $0\,K$.

Cation distribution, as obtained from above method, is given in Table 3. It can be seen that the observed and calculated intensity ratios I_{220}/I_{400}, I_{400}/I_{422} and I_{220}/I_{422} fairly match with each other with minimum values of agreement factor. Cation distribution suggests that the Zn^{2+} ions occupy tetrahedral — A-site while Ni^{2+} ions prefer octahedral — B-site. Most of the Mn^{2+} ions prefer the A-site and only a small fraction occupies B-site. Nearly 80% Ce^{3+} ions replaces Fe^{3+} ions at octahedral — B-site and the remaining 20% replaces at tetrahedral — A-site.

Figure 4(a) shows the variation of mean ionic radii (r_A and r_B) of the tetrahedral — A and octahedral — B sites, respectively, by using the equations taken from literature.[47] Figure 4(a) implies that the introduction of Ce^{3+} ions increases the mean ionic radii "r_A" from 0.792 to 0.801 Å and

Table 3. Cation distribution and intensity ratio calculations for $Ni_{0.35}Mn_{0.35}Zn_{0.3}Fe_{2-x}Ce_xO_4$.

| 'x' | Cation distribution | | | | | | | | Intensity ratios | | | | | |
| | A-Site | | | | B-Site | | | | (220/400) | | (400/422) | | (220/422) | |
	Mn	Zn	Ce	Fe	Ni	Mn	Ce	Fe	Obs.	Cal.	Obs.	Cal.	Obs.	Cal.
0.0	0.3	0.3	0.0	0.4	0.35	0.05	0.0	1.6	1.442	1.434	2.009	2.012	2.898	2.886
0.025	0.3	0.3	0.005	0.395	0.35	0.05	0.02	1.58	1.432	1.423	2.017	2.027	2.889	2.884
0.050	0.3	0.3	0.01	0.39	0.35	0.05	0.04	1.56	1.428	1.412	2.012	2.038	2.873	2.877
0.075	0.3	0.3	0.015	0.385	0.35	0.05	0.06	1.54	1.409	1.400	2.037	2.051	2.870	2.872
0.1	0.3	0.3	0.02	0.38	0.35	0.05	0.08	1.52	1.392	1.390	2.055	2.064	2.861	2.868
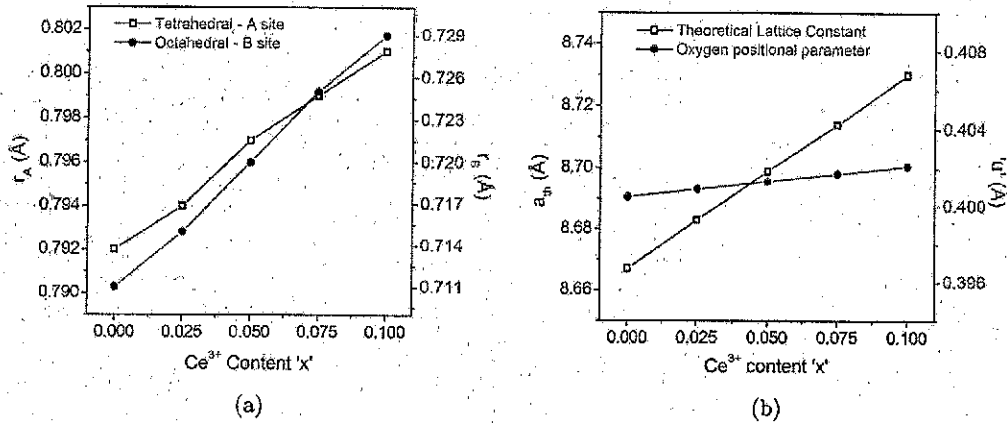
Fig. 4. (a): variation of mean ionic radii at tetrahedral — A (r_A) and octahedral — B (r_B) site, (b) variation of theoretical lattice constant (a_{th}) and oxygen positional parameter (u) for $Ni_{0.35}Mn_{0.35}Zn_{0.3}Fe_{2-x}Ce_xO_4$.

"r_B" from 0.711 Å to 0.729 Å. This increasing behavior of mean ionic radii is related to the higher ionic radii of Ce^{3+} ion which replaces Fe^{3+} ions having relatively smaller ionic radii. Theoretical lattice constant "a_{th}" and oxygen positional parameter "u" for all the composition were computed by using the following relations[48]:

$$a_{th} = \frac{8}{3}\left[\frac{1}{\sqrt{3}}(r_A + R_0) + (r_B + R_0)\right], \quad (8)$$

$$u = \left[\frac{1}{4} + (r_A + R_0)\frac{1}{\sqrt{3a}}\right], \quad (9)$$

where "r_A" and "r_B" are the mean ionic radii of tetrahedral — A and octahedral — B sites, respectively, and R_0 is the radius of oxygen ion. Figure 4(b) represents the variation of theoretical lattice constant "a_{th}" and oxygen parameter "u" as a function of Ce^{3+} dopant "x". Theoretical lattice parameter "a_{th}" increases from 8.6670 Å to 8.7302 Å which is in good agreement with the variation of calculated lattice parameter. Oxygen positional

parameter "u" increases with the addition of Ce^{3+} ions in Ni–Mn–Zn–Fe–O lattice. This increase in oxygen parameter may be associated to the shifting of origin towards tetrahedral — A-site due to the dilution of Fe^{3+} ions at octahedral — B-site which causes the distortion in the crystal lattice.[49]

Close morphology and particle size of the Ce^{3+}-doped Ni–Mn–Zn ferrites were studied by using high resolution TEM. TEM images of the samples $x = 0.0$, 0.05 and 0.1 are represented in Figs. 5(a)–5(c), respectively. Figure 5(d) shows the SEAD pattern of the sample $x = 0.05$. TEM images clearly show the particles are in spherical shape with almost uniform size. Particle size distribution was estimated by using the software Image J. Inset of Figs. 5(a)–5(c) shows the particle size distributions histograms. Particle size increases from 22.8 nm to 26.1 nm with the increasing percentage of Ce^{3+} ions. Results obtained from TEM analysis are closely consistent with XRD analysis. Bright spotted rings observed in the SEAD pattern confirm the polycrystalline nature of the samples.
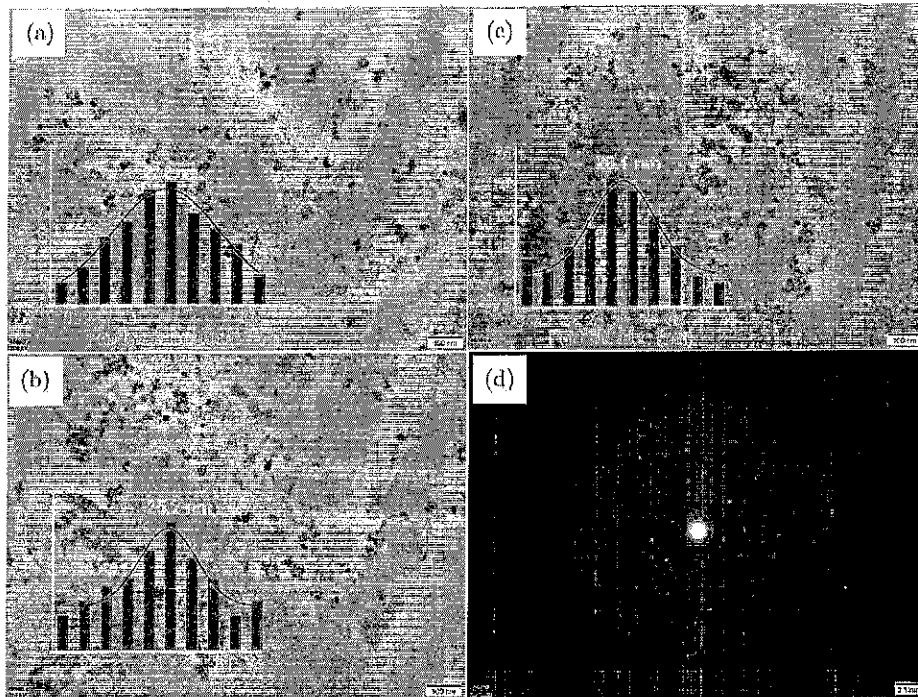
Fig. 5. TEM images of $Ni_{0.35}Mn_{0.35}Zn_{0.3}Fe_{2-x}Ce_xO_4$ (a) $x = 0.0$, (b) $x = 0.05$, (c) $x = 0.1$ and (d) SEAD pattern of $Ni_{0.35}Mn_{0.35}Zn_{0.3}Fe_{1.95}Ce_{0.05}O_4$.

Figure 6(a) represents the Fourier transform infrared spectra of all the samples recorded in the wavenumber range of 350–4000 cm^{-1} and Fig. 6(b) shows the expanded view in the range of 350–800 cm^{-1}. Absorption bands observed near the wavenumber range 3440 cm^{-1}, 1590 cm^{-1} and 1380 cm^{-1} representing the stretching and bending vibrations of absorbed water.[50,51] Characteristic absorption bands (metal-oxygen) of spinel crystals are observed in the range 350–800 cm^{-1}.[52,53] The two distinct bands observed in the range 350–800 cm^{-1} are assigned to the M-O vibrations of tetrahedral — A and octahedral — B sites.[54] Metal cations at tetrahedral site vibrates along the line joining to neighboring oxygen ions, while as cations at octahedral site vibrates in perpendicular direction to the line joining to oxygen ion.[55] The high-frequency band (ν_1) corresponds to the tetrahedral
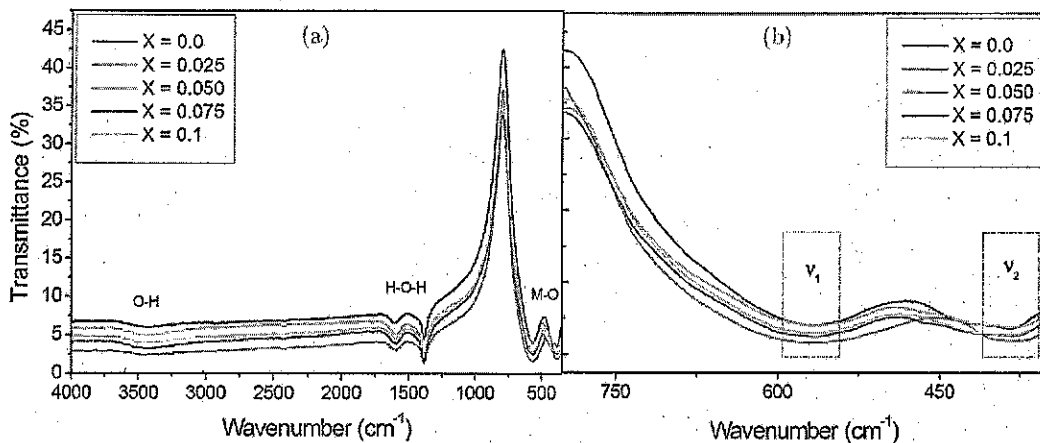

Fig. 6. (a): FTIR spectra and (b) FTIR spectra expanded for the region 350 to 800 cm^{-1} for the series $Ni_{0.35}Mn_{0.35}Zn_{0.3}Fe_{2-x}Ce_xO_4$.

— A-site is observed in the range 565–580 cm^{-1} and the low-frequency band (ν_2) corresponding to octahedral — B-site is observed in the range 370–385 cm^{-1}. The band positions ν_1 and ν_2 are listed in Table 4. The addition of Ce^{3+} ions shifts the band positions slightly towards higher frequency region which implies that Ce^{3+} ions are incorporated in the crystal lattice at both tetrahedral — A and octahedral — B sites. Force constants "K_t" and "K_0" for tetrahedral — A and octahedral — B sites were computed by using the relations suggested by Waldron.[52] Molecular weights obtained from cation distribution and force constants of tetrahedral — A, octahedral — B sites are given in Table 4.

Elastic constants and modulus define the strength of the materials at different strain conditions and hence have a prime importance in industrial applications. Force constants and crystallographic parameters were used to estimate the elastic parameters of Ce^{3+}-doped Ni–Mn–Zn ferrite nanoparticles. According to Waldron,[52] the cubic crystals, possessing isotropic nature, have the stiffness constant $C_{11} = C_{12}$. Thus, for spinel ferrites, bulk modulus is $B = (C_{11} + 2C_{12})/3 = C_{11}$. The stiffness constant and elastic moduli were calculated using the following relations[56–58]:

$$C_{11} = \frac{K_{av}}{a}, \tag{10}$$

$$V_{\rm m} = \left[\frac{1}{3}\left(\frac{2}{V_S^3} + \frac{1}{V_l^3}\right)\right]^{-1/3} \tag{11}$$

where V_m is mean wave velocity, $V_S = V_l/\sqrt{3}$ is transverse wave velocity and $V_l = \sqrt{(C_{11}/\rho)}$ is the longitudinal wave velocity.

Rigidity modulus:

$$G = \rho V_s^2. \tag{12}$$

Poisson's ratio:

$$\sigma = \frac{3B - 2G}{6B + 2G}. \tag{13}$$

Young's modulus:

$$E = (1 + \sigma)2G. \tag{14}$$

Table 4 represents the values of force constants K_O, K_T, elastic moduli (B, E and G) and Poisson's ratio (σ) computed by using above relations. The constant value of Poisson's ration ($\sigma = 0.35$) representing the isotropic elastic behavior is in good agreement with the literature values of spinel ferrites. Literature reports suggest that the good elastic behavior can be achieved when Poisson's ratio must lie in the range of -1–0.5.[59–61] Values of various elastic moduli are in general associated to the inter-ionic bondings. Bhaskar and his co-worker suggested that the enriched elastic parameters can be obtained when the inter-ionic bonding is strong.[62] In this study, values of bulk modulus, Young's modulus and rigidity modulus show increasing trend with replacement of Fe^{3+} ions by Ce^{3+} ions. Increasing behavior of various elastic parameters may be attributed to the increasing

Table 4. Elastic parameters of Ni$_{0.35}$Mn$_{0.35}$Zn$_{0.3}$Fe$_{2-x}$Ce$_x$O$_4$.

'x'	0.0	0.025	0.050	0.075	0.1
M_A (gm/mol)	77.64	78.06	78.48	78.90	79.32
M_B (gm/mol)	157.44	159.13	160.81	162.50	164.18
ν_1 (cm^{-1})	569.83	571.57	574.65	577.34	579.36
ν_2 (cm^{-1})	371.45	372.89	374.72	379.52	383.57
$K_T \times 10^5$ (dynes/cm)	192.10	194.32	197.48	200.41	202.89
$K_O \times 10^5$ (dynes/cm)	115.35	117.49	119.90	124.28	128.27
$K_{av} \times 10^5$ (dynes/cm)	153.72	155.91	158.69	162.34	165.58
V_l (m/s)	5900	5929	5967	6023	6068
V_t (m/s)	3406	3423	3445	3477	3503
B (GPa)	182.78	185.30	188.60	192.84	196.66
G (GPa)	60.93	61.77	62.87	64.28	65.55
σ	0.35	0.35	0.35	0.35	0.35
E (GPa)	164.50	166.77	169.74	173.56	177.00
V_m (m/s)	3782	3800	3825	3860	3889
θ_D (K) (Waldron)	676	679	682	687	692

inter-ionic bonding between the ions of $Ni_{0.35}Mn_{0.35}Zn_{0.3}Fe_{2-x}Ce_xO_4$.

The relation, as suggested by Waldron, is used to estimate the Debye temperature of the following samples[52]:

$$\theta_D = \frac{\hbar C}{k_B}\nu_{avg}, \qquad (15)$$

where $\nu_{avg.} = (\nu_1 + \nu_2)/2$ and $(\hbar C/k_B) = 1.438$. Obtained values of Debye's temperature from above relation are given in Table 4. Debye temperature increases from 676 K to 692 K with the introduction of Ce^{3+} ions in Ni–Mn–Zn–Fe–O crystals. This can be explained on the basis of specific heat theory.[63] Increased positive charge carriers with the increasing concentration of Ce^{3+} ions may increase the Debye temperature.

4. Conclusions

Nanoparticles of $Ni_{0.35}Mn_{0.35}Zn_{0.3}Fe_{2-x}Ce_xO_4$ spinel ferrite system were successfully obtained using sol–gel approach. XRD patterns reveal the single phase cubic spinel structure of the samples with space group Fd-3m. Phase purity confirms the successful introduction of Ce^{3+} ions in Ni–Mn–Zn–Fe–O crystal lattice. W–H analysis indicates that the tensile type strain induced in the crystal lattice. Cation distribution analysis suggests that the Zn^{2+} ions occupy tetrahedral — A-site while Ni^{2+} ions prefer octahedral — B-site. Most of the Mn^{2+} ions prefer the A-site and only a small fraction occupies B-site and on the other hand majority of the Ce^{3+} ions prefer octahedral — B-site. HR-TEM images confirm the nanoscale dimension of particles with small agglomeration. FTIR spectra show the main characteristic absorption bands (metal-oxygen) of spinel crystals are observed in the range 350–800 cm^{-1}. Stiffness constant and elastic moduli show increasing behavior with the increasing concentration of Ce^{3+} ions. Increased mechanical strength makes these materials suitable for industrial applications.

References

1. S. Thota, S. C. Kashyap, S. K. Sharma and V. R. Reddy, *Mater. Sci. Eng. B* **206**, 69 (2016).
2. A. A. Sattar, H. M. El-Sayed, K. M. El-Shokrofy and M. M. El-Tabey, *J. Appl. Sci.* **5**, 162 (2005).
3. J. Pei, Z. Wang, Y. Gao and H. Zhang, *Curr. Appl. Phys.* **19**, 440 (2019).
4. A. Safari, K. H. Gheisari and M. Farbod, *J. Magn. Magn. Mater.* **488**, 165369 (2019).
5. T. Dippong, E. A. Levei, O. Cader, F. Goga, L. B. Tudoran and G. Borodi, *J. Anal. Appl. Pyrol.* **128**, 121 (2017).
6. T. Dippong, E. A. Levei, O. Cadar, A. Mesaros and G. Borodi, *J. Anal. Appl. Pyrol.* **125**, 169 (2017).
7. T. Dippong, E. A. Levei, I. G. Deac, F. Goga and O. Cadar, *J. Anal. Appl. Pyrol.* **144**, 104713 (2019).
8. H. Anwar and A. Maqsood, *Mater. Res. Bull.* **49**, 426 (2014).
9. S. Atiq, M. Majeed, A. Ahmad, S. K. Abbas, M. Saleem, S. Riaz and S. Naseem, *Ceram. Int.* **43**, 2486 (2017).
10. Y. Wang, X. Wu, W. Zhang and W. Chen, *J. Magn. Magn. Mater.* **398**, 90 (2016).
11. A. R. Bueno, M. L. Gregori and M. C. S. Nobrega, *Mater. Chem. Phys.* **105**, 229 (2007).
12. K. Jalaih and K. V. Babu, *J. Magn. Magn. Mater.* **423**, 275 (2017).
13. S. Ramesh, B. Chandra Shekhar, P. S. V. Subba Rao and B. Parvatheeswara Rao, *Ceram. Int.* **40**, 8729 (2014).
14. T. Dippong, O. Cadar, E. A. Levei and I. G. Deac, *J. Magn. Magn. Mater.* **498**, 166168 (2020).
15. T. Dippong, O. Cadar, E. A. Levei, I. G. Deac and G. Borodi, *Ceram. Int.* **44**, 10478 (2018).
16. T. Dippong, O. Cadar, I. G. Deac, M. Lazar, G. Borodi and E. A. Levei, *J. Alloys Compd.* **828**, 154409 (2020).
17. T. Roman, A. Pui, A. V. Lukacs, N. Cimpoesu, S. Lupescu, A. I. Borhan, K. Kordatos, A. Ntziouni, P. Postolache, M. Zaharia, S. Stanciu and L. Mitoseriu, *Ceram. Int.* **45**, 17243 (2019).
18. M. R. Nasrabadi, M. Behpour, A. S. Nasab and M. R. Jeddy, *J. Mater. Sci: Mater. Electron.* **27**, 11691 (2016).
19. M. A. Almesssiere, A. D. Korkmaz, Y. Slimani, M. Nawaz, S. Ali and A. Bayakal, *Ceram. Int.* **45**, 3449 (2019).
20. H. Hussain, N. Amin and M. I. Arshad, *Ceram. Int.* **47**, 3401 (2021).
21. M. Hashim, A. Ahmed, S. A. Ali, S. E. Shirsath, M. M. Ismail, R. Kumar, S. Kumar, S. S. Meena and D. Ravinder, *Ceram. Int.* **834**, 155089 (2020).
22. M. A. Malana, R. B. Qureshi, M. N. Ashiq and Z. I. Zafar, *Mater. Res. Bull.* **48**, 4775 (2013).
23. M. Rivero, A. D. Campo, A. Mayoral, E. Mazario, J. S. Marcos and A. M. Bonilla, *RSC Adv.* **6**, 40067 (2016).
24. A. K. Singh, T. C. Goel and R. G. Mendiratta, *Solid State Commun.* **125**, 121 (2003).
25. R. H. Kadam, A. Karim, A. B. Kadam, A. S. Gaikwad and S. E. Shirsath, *Int. Nano. Lett.* **2**, 28 (2012).

26. M. V. Chaudhari, S. E. Shirsath, A. B. Kadam, R. H. Kadam, S. B. Shelke and D. R. Mane, *J. Alloys Compd.* **552**, 443 (2013).

27. D. L. Sekulic, Z. Z. Lazarevic, M. V. Sataric, C. D. Jovalekic and N. R. Romcevic, *J. Mater. Sci: Mater. Electron.* **26**, 1291 (2015).

28. R. H. Kadam, A. R. Birajdar, M. L. Mane and S. E. Shirsath, *J. Appl. Phys.* **112**, 043902 (2012).

29. M. U. Rana, M. Islam and T. Abbas, *J. Mater. Chem. Phys.* **65**, 3 (2000).

30. S. E. Shirsath, R. H. Kadam, M. L. Mane, A. Ghesami, Y. Yasukawa, X. Liu and A. Morisako, *J. Alloys Compd.* **575**, 145 (2013).

31. M. Rabiei, A. Palevicius, A. Monshi, S. Nasiri, A. Vilkauskas and G. Janusas, *Nanomaterials* **10**, 1627 (2020).

32. D. Nath, F. Singh and R. Das, *Mater. Chem. Phys.* **239**, 122021 (2019).

33. R. Jacob and J. Isac, *Int. J. Chem. Stud.* **2**, 12 (2015).

34. S. S. Choudhari, S. R. Wadgane, B. P. Gaikwad, S. S. Satpute, K. M. Batoo, O. M. Aldossary, S. E. Shirsath and R. H. Kadam, *Ceram. Int.* **47**, 6494 (2021).

35. W. H. Hall, *Acta Metall.* **1**, 22 (1953).

36. B. E. Warren and B. L. Averbach, *J. Appl. Phys.* **23**, 497 (1952).

37. B. R. Kumar and B. Hymavathi, *J. Asian Ceram. Soc.* **5**, 94 (2017).

38. R. H. Kadam, R. B. Borade, M. L. Mane, D. R. Mane, K. M. Batoo and S. E. Shirsath, *RSC Adv.* **10**, 27911 (2020).

39. H. Irfan, M. Radik and S. Anand, *J. Asian Ceram. Soc.* **6**, 54 (2018).

40. M. A. Tagliente and M. Massaro, *Nucl. Instrum. Methods Phys. Res. B* **266**, 1055 (2008).

41. H. Nikmanesh, P. Kameli, S. M. Asgarian, S. Karimi, M. Moradi, Z. Kargar, J. Venture and B. Bordlao, *RSC Adv.* **7**, 22320 (2017).

42. H. Furuhashi, M. Inagaki and S. Naka, *J. Inorg. Nucl. Chem.* **35**, 3009 (1973).

43. E. F. Bertaut, *J. Phys. Radium* **12**, 252 (1951).

44. R. H. Kadam, K. Desai, S. R. Kadam and S. E. Shirsath, *Solid State Sci.* **26**, 31 (2013).

45. B. D. Culity, *Elements of X-ray Diffraction* (Addison-Wesley Publishing Company, Reading, Massachusetts, USA, 1956), pp. 99.

46. R. H. Kadam, K. Desai, V. S. Shinde, M. Hashim and S. E. Shirsath, *J. Alloys Compd.* **657**, 487 (2016).

47. R. K. Sharma, V. Sebastian, N. Lakshmi, K. Venugopalan, V. R. Reddy and A. Gupta, *Phys. Rev. B* **75**, 144419 (2007).

48. S. K. Gurav, S. E. Shirsath, R. H. Kadam and D. R. Mane, *Powder Technol.* **235**, 485 (2013).

49. G. Fagherazzi and F. Garbassi, *J. Appl. Crystallogr.* **5**, 18 (1972).

50. S. J. Haralkar, R. H. Kadam, S. S. More, S. E. Shirsath, M. L. Mane, S. D. Patil and D. R. Mane, *Mater. Res. Bull.* **48**, 1189 (2013).

51. M. Mozaffari, S. Manouchehri, M. H. Yousefi and J. Amighian, *J. Magn. Magn. Mater.* **322**, 383 (2010).

52. R. Waldron, *Phys. Rev.* **99**, 1727 (1955).

53. M. H. Abdellatif, A. A. Azab and M. Salerno, *Mater. Res. Bull.* **97**, 260 (2018).

54. S. K. Gurav, S. E. Shirsath, R. H. Kadam, S. M. Patange, K. S. Lohar and D. R. Mane, *Mater. Res. Bull.* **48**, 3530 (2013).

55. A. B. Gadkari, T. J. Shinde and P. N. Vasambekar, *Mater. Chem. Phys.* **114**, 505 (2009).

56. K. Pubby, K. V. Babu and S. B. Narang, *Mater. Sci. Eng. B* **255**, 114513 (2020).

57. M. A. Ali, M. N. I. Khan, M. M. Hossain, F. U. Z. Chowdhury, M. N. Hossain, R. Rshid and M. A. Hakim, *Mater. Res. Express* **7**, 036101 (2020).

58. K. B. Modi, S. J. Shah, N. B. Pujara, T. K. Pathak, N. H. Vasoya and I. G. Jhala, *J. Mol. Struct.* **1049**, 250 (2013).

59. D. Boukkeze, J. Massoudi, W. Hzez, M. Smari, A. Bougoffa, K. Khirouni, E. Dhahri and L. Bessais, *RSC Adv.* **9**, 40940 (2019).

60. K. B. Modi, M. K. Rangolia, M. C. Chhantbar and H. H. Joshi, *J. Mater. Sci.* **41**, 7308 (2006).

61. K. B. Modi, M. C. Chhantbar and H. H. Joshi, *Ceram. Int.* **32**, 111 (2006).

62. A. Bhaskar and S. R. Murthy, *J. Magn. Magn. Mater.* **355**, 100 (2014).

63. S. A. Mazen, S. F. Mansour, E. Dhahri, H. M. Zaki and T. A. Elmosalami, *J. Alloys Compd.* **470**, 294 (2009).

2020-21.

9128